Available online at www.sciencedirect.com
ScienceDirect
Journal of Sound and Vibration 309 (2008) 293–306
JOURNAL OF SOUND AND VIBRATION
www.elsevier.com/locate/jsvi

Near-field acoustic intensity measurements using an accelerometer-based underwater intensity vector sensor

K. Kim*, G.C. Lauchle, T.B. Gabrielson

Graduate Program in Acoustics, The Pennsylvania State University, University Park, Pennsylvania, PA 16802, USA

Received 31 January 2006; received in revised form 7 October 2006; accepted 18 July 2007
Available online 11 September 2007

Abstract

An accelerometer-based underwater acoustic intensity vector sensor is used to measure the acoustic nearfield of a single spherical source, and a pair of sources that vibrate in or out of phase with each other. The intensity sensor consists of co-located pressure and inertial sensors within a neutrally buoyant probe body. The design of this probe has been published previously. The measurements were performed in a large tank at a frequency of 5 kHz for two sources of different sizes, corresponding to ka values of 0.7 and 1.2 respectively, where k is acoustic wavenumber and a is the source radius. By way of validation, the acoustic intensity field from two closely spaced, interacting spherical radiators is predicted using the exact theory of the translational addition theorem for spherical wave functions. The predictions using this theory compare favorably well with the measured intensity field. Beam pattern and calibration data obtained for the intensity sensor suggest that underwater acoustic intensity generated by simple and complex sources can be measured to an accuracy of ± 1 dB provided that ka is less than approximately 0.2.

1. Introduction

In the areas of acoustic radiation and noise control, understanding the nearfield of complex radiators that may be composed of several interacting sources is essential. Acoustic pressure measurements performed near any radiator, regardless of complexity, are contaminated by non-propagating evanescent waves rendering such measurements inaccurate for source localization or determination of sound power. Acoustic intensity measurement is therefore the most frequently applied, and accepted technique in this area. Intensity provides a vector description of the radiation pattern that helps in the localization and ordering of sources and sinks. The active intensity is acoustic power per unit area, so intensity measurements performed over any measurement surface area that surrounds the radiator can be used to determine the power of the radiator.

A theoretical analysis on sound energy flux was first carried out by Enns and Firestone [1] and a two-pressure-microphone technique was introduced by Bolt and Petrauskas [2] for the measurement of acoustic impedance of material samples. Several different types of instruments for sound power measurements were

*Corresponding author. Department of Biomedical Engineering, University of Michigan, 2200 Bonisteel Blvd., Ann Arbor, MI 48109, USA. Tel.: +1 734 763 5448.
E-mail address: kangkim@umich.edu (K. Kim).

0022-460X/$ - see front matter © 2007 Elsevier Ltd. All rights reserved.
doi:10.1016/j.jsv.2007.07.024

developed, including an acoustic wattmeter with a ribbon velocity microphone and a pressure microphone, and hot-wire anemometer with a pressure microphone [3–5]. Schultz [6] built an acoustic wattmeter using the two-pressure-microphone technique employed by Bolt and Petrauskas [2]. It was in the late 1970s that Fahy [7] and Chung [8] showed, separately, that intensity is proportional to the cross-spectrum between two pressure-microphone outputs. This technique, along with the development of FFT analyzers and phase-matched microphone pairs, marked the beginning of reliable in-air intensity measurements.

Most intensity sensors for in-air use are based on the two-microphone technique [9]. The method has not enjoyed very much success in underwater applications because of the difficulty in finding two piezoelectric hydrophones that are reasonably well phase- and amplitude-matched over a broad range of frequencies. More emphasis, therefore, has been placed on measuring underwater acoustic particle velocity and intensity directly using neutrally buoyant inertial sensors. Leslie et al. [10] published the first account of such a sensor years after the prototype was built in 1941. A two-component inertial vector sensor design, using moving-coil transducers, was developed by Bauer and DiMattia [11]. Simultaneous measurements of infrasonic (0.5–20 Hz) acoustic pressure and particle velocity made by the Swallow Floats system are analyzed and the limits to performance of the system are described by D'Sapain et al. [12]. Gabrielson, Gardner, and Garrett built and successfully tested a neutrally buoyant inertial sensor consisting of a glass-microballoon-and-epoxy composite cast surrounding a small, commercial geophone [13,14]. A u–u probe using two closely spaced velocity sensors can be also used to measure higher-order acoustic variables like density fluctuations [15,16]. These types of sensors, composed of accelerometers or geophones encased in neutrally buoyant shells, are not limited by finite-difference and phase mismatch errors associated with two pressure sensing probes, i.e., p–p probes [9].

Kim et al. [17] built and successfully tested a neutrally buoyant intensity sensor consisting of a pressure transducer in the form of a hollow piezoceramic cylinder and a pair of miniature accelerometers mounted inside of the cylinder (p–a probe). The response of this intensity probe was determined by comparison with the response of a reference hydrophone in a predominantly reactive acoustic field. In this paper, the practical use of this sensor is demonstrated in a more complicated field containing both active and reactive components. Simple 2-D acoustic intensity fields were created in a small laboratory water tank by driving a single spherical source in one case, and a pair of spherical sources together in another. These fields were chosen because of their generic interest in acoustic radiation, and also because they are amenable to exact theoretical prediction [18–20]. This provides a theoretical benchmark in which the intensity measurements can be validated.

2. Theoretical predictions

2.1. Acoustic intensity field near two closely spaced spherical sources

The classic solution to the acoustic field of two identical compact sources assumes that each of the sources acts independently—the field from one source does not affect the radiation characteristics of the other [21–24]. Therefore, the sound field due to either of the sources at any point in space is the same as it would be if the other were not there. For small separation between sources, this is not, in general, true. Using the Translational Addition Theorem for Spherical Wave Functions (TATSWF), Thompson [18–20] found an analytical solution for the acoustic coupling between two non-compact spherical sources. Based on his derivation, a numerical solution is derived (and evaluated) for the acoustic intensity field produced by two closely spaced, spherical sound sources of different sizes. Experimental data, described in the next section, are compared with the numerical predictions of this solution.

Consider two time-harmonic, spherical sound sources of different sizes, separated by a center-to-center distance r_o in a free space (see Fig. 1). The medium is assumed to be homogeneous and isotropic. Since the configuration is axisymmetric about the $\theta = 0$ axis, the surface velocity distribution of each source, in general, can be expressed as a Legendre series [19]:

$$v(a, \theta_1) = V_o \sum_{n=0}^{\infty} v_n P_n(\cos\ \theta_1) \tag{1}$$

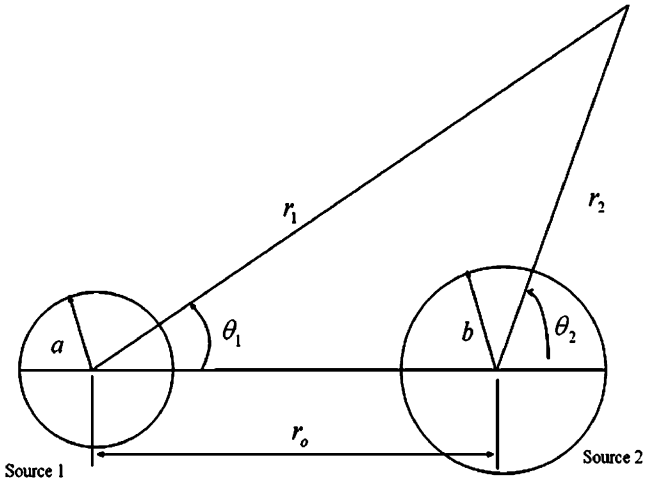

Fig. 1. Configuration of the two finite-sized spherical sources as illustrated by Thompson [18].

and

$$u(b,\theta_2) = U_o \sum_{n=0}^{\infty} u_n P_n(\cos\ \theta_2), \tag{2}$$

where $v(a,\theta_1)$ is the velocity of source 1 and $u(b,\theta_2)$ is the velocity of source 2. V_o and U_o are arbitrary velocity amplitudes, and P_n are Legendre polynomials. The acoustic pressure distribution in space of either source, due to the prescribed velocity distribution of that source, can then be expanded into a series of outgoing spherical wave functions using spherical Hankel function of the second kind [19]:

$$p_1(r_1,\theta_1) = P_{01} \sum_{n=0}^{\infty} a_n h_n^{(2)}(kr_1) P_n(\cos\ \theta_1) \tag{3}$$

and

$$p_2(r_2,\theta_2) = P_{02} \sum_{n=0}^{\infty} b_n h_n^{(2)}(kr_2) P_n(\cos\ \theta_2), \tag{4}$$

where a_n and b_n are unknown, dimensionless, complex coefficients to be related to the known, dimensionless, velocity coefficients v_n and u_n, and P_{10} and P_{20} are arbitrary pressure amplitudes. $h_n^{(2)}$ are spherical Hankel function of the second kind.

It should be noted that even if each of the sources pulsates in a single spherical mode, the total pressure radiated by each source needs to be expressed in the form of an infinite sum of modes due to the presence of the other source. The multiple scattering between the two sources produces the infinite number of spherical modes for each source. To match the boundary condition on the surface of each source, it is desirable to express the pressure due to source 1 in coordinates centered at source 2 and the pressure due to source 2 in coordinates centered at source 1. This transformation of the functional form of the pressure is accomplished by the TATSWF. Employing the expression of the translated progressive spherical wave modes from one coordinate to the other, the pressure field in the coordinates centered at source 1 can be expressed as a function of the coordinates centered at source 2:

$$p_1(r_2,\theta_2) = P_{01} \sum_{m=0}^{\infty} A_m j_m(kr_2) P_m(\cos\ \theta_2), \quad \text{for } r_2 < r_o \tag{5}$$

and

$$p_2(r_1,\theta_1) = P_{02}\sum_{m=0}^{\infty} B_m j_m(kr_1)P_m(\cos\ \theta_1), \quad \text{for } r_1 < r_o, \tag{6}$$

where r_o is the distance between the two sources. The dimensionless coefficients A_m and B_m, above, are related to the coefficients a_n and b_n in Eqs. (3) and (4) in the functional forms:

$$A_m = K_m\sum_{n=0}^{\infty} a_n \Lambda_n^{(m)}(kr_o) \tag{7}$$

and

$$B_m = K_m\sum_{n=0}^{\infty}(-1)^{n+m} b_n \Lambda_n^{(m)}(kr_o), \tag{8}$$

where the constant K_m is given by

$$K_m = \frac{1\ 3\ 5\cdots(2m+1)}{m!} \tag{9}$$

and the weighting factor $\Lambda_n^{(m)}(kr_o)$ is a function of the outgoing wave function, the spherical Hankel function of the second kind.

The boundary condition on the surface of each source is [18,19]

$$\frac{1}{k\rho c}\frac{\partial}{\partial r_1}(p_1(r_1,\theta_1)+p_2(r_1,\theta_1))_{r_1=a} = v(a,\theta_1) = V_o\sum_{n=0}^{\infty} v_n P_n(\cos\ \theta_1) \tag{10}$$

and

$$\frac{1}{k\rho c}\frac{\partial}{\partial r_2}(p_1(r_2,\theta_2)+p_2(r_2,\theta_2))_{r_2=b} = u(b,\theta_2) = U_o\sum_{n=0}^{\infty} u_n P_n(\cos\ \theta_2), \tag{11}$$

where k is wave number, ρ is density, and c is sound speed. $p_1(r_1,\theta_1)$ and $p_2(r_1,\theta_1)$ are pressure of corresponding sources in coordinates centered at source 1, and $p_1(r_2,\theta_2)$ and $p_2(r_2,\theta_2)$ are pressure of corresponding sources in coordinates centered at source 2. Substituting Eqs. (3)–(6) into Eqs. (10) and (11), and matching each individual mode separately produces the equations [18,19]:

$$P_{02}[j_m'(ka)/h_m^{(2)'}(ka)]K_m\sum_{n=0}^{\infty} b_n\Lambda_n^{(m)}(kr_o) + P_{01}a_m = -jV_o\rho c v_m/h_m^{(2)'}(ka) \tag{12}$$

and

$$P_{01}[j_m'(kb)/h_m^{(2)'}(kb)]K_m\sum_{n=0}^{\infty} a_n b_n\Lambda_n^{(m)}(kr_o) + P_{02}b_m = -jU_o\rho c u_m/h_m^{(2)'}(kb), \tag{13}$$

where the prime on the superscript denotes the first-order derivative with respect to the argument.

P_{01} and P_{02} are arbitrary pressure amplitudes. The constant K_m and the weighting factor $\Lambda_n^{(m)}(kr_o)$ generated in the process of coordinate transformation (TATSWF) can be found in Thompson [18–20]. Note that the equations above are valid for all integer values m. If both indices, n and m, are truncated at a value of $N-1$, a $2N\times 2N$ complex matrix equation results that can be solved for N values of a_n and N values of b_n. For the range $kr_o<12$, Thompson [18] suggested an empirical number, $N = 2(ka)8$ as the necessary number of terms for adequate convergence of the pressure series. This value is for the case of equal sized sources, where k is the acoustic wavenumber and a is the radius of the sound source. Once the matrix equation is solved for the coefficients a_n and b_n, the acoustic pressure everywhere in the field is determined.

Through Euler's equation, the acoustic particle velocity is then calculated from the acoustic pressure. The particle velocities in the radial direction, referenced to each coordinate, are:

$$v_{1r_1}(r_1,\theta_1) = V_{01}\sum_{n=0}^{\infty} a_n h_m^{(2)'}(kr_1)P_n(\cos\ \theta_1) \tag{14}$$

and

$$v_{2r_2}(r_2,\theta_2) = V_{02}\sum_{n=0}^{\infty} b_n h_m^{(2)'}(kr_2)P_n(\cos\ \theta_2), \tag{15}$$

where $V_{01} = jP_{01}/\rho c$ and $V_{02} = jP_{02}/\rho c$. The prime on the spherical Hankel function denotes the first-order derivative with respect to the argument of the function. The particle velocities in the tangential direction, referenced to each coordinate, are:

$$v_{1\theta_1}(r_1,\theta_1) = V_{01}\left(\frac{-\sin\ \theta_1}{kr_1}\right)\sum_{n=0}^{\infty} a_n h_n^{(2)}(kr_1)P_n'(\cos\ \theta_1) \tag{16}$$

and

$$v_{2\theta_2}(r_2,\theta_2) = V_{02}\left(\frac{-\sin\ \theta_2}{kr_2}\right)\sum_{n=0}^{\infty} b_n h_n^{(2)}(kr_2)P_n'(\cos\ \theta_2), \tag{17}$$

where the prime on the Legendre function denotes the first-order derivative with respect to its argument. Each velocity in the radial direction and the tangential direction is decomposed into x and y components in Cartesian coordinates and vector-summed, i.e.,

$$v_{1x} = v_{1r}\ \cos(\theta_1) - v_{1\theta}\ \sin(\theta_1), \tag{18}$$

$$v_{1y} = v_{1r}\ \sin(\theta_1) + v_{1\theta}\ \cos(\theta_1), \tag{19}$$

$$v_{2x} = v_{2r_2}\ \cos(\theta_2) - v_{2\theta_2}\ \sin(\theta_2), \tag{20}$$

$$v_{2y} = v_{2r_2}\ \sin(\theta_2) - v_{2\theta_2}\ \cos(\theta_2). \tag{21}$$

The sum of Eqs. (18) and (20) gives the total acoustic particle velocity in the x-direction, and the sum of Eqs. (19) and (21) gives the acoustic particle velocity in the y-direction. By definition, [9] multiplying the total particle velocity in each direction and the total acoustic pressure results in the total acoustic intensity in the x- and y-directions, respectively.

2.2. Intensity of two sources that are pulsating in the fundamental mode

As an example, consider each source pulsating in only its fundamental breathing mode. Source 1 is vibrating uniformly in the radial direction with velocity v_o, and source 2 is vibrating uniformly in the radial direction with velocity u_o. Because $m = 0$ in this example, the right-hand terms in Eqs. (12) and (13) are zero for $m > 1$. If, for example, m and n, are each truncated at $N = 3$, the matrix equation derived from Eqs. (12) and (13) has the form:

$$\begin{bmatrix} 1 & 0 & 0 & C_0^a K_0 \Lambda_0^{(o)} & -C_0^a K_0 \Lambda_1^{(o)} & C_0^a K_0 \Lambda_2^{(o)} \\ 0 & 1 & 0 & -C_1^a K_1 \Lambda_0^{(1)} & C_1^a K_1 \Lambda_1^{(1)} & -C_1^a K_1 \Lambda_2^{(1)} \\ 0 & 0 & 1 & C_2^a K_2 \Lambda_0^{(2)} & -C_2^a K_2 \Lambda_1^{(2)} & C_2^a K_2 \Lambda_2^{(2)} \\ C_0^b K_0 \Lambda_0^{(o)} & C_0^b K_0 \Lambda_1^{(o)} & C_0^b K_0 \Lambda_2^{(o)} & 1 & 0 & 0 \\ C_1^b K_1 \Lambda_0^{(1)} & C_1^b K_1 \Lambda_1^{(1)} & C_1^b K_1 \Lambda_2^{(1)} & 0 & 1 & 0 \\ C_2^b K_2 \Lambda_0^{(2)} & C_2^b K_2 \Lambda_1^{(2)} & C_2^b K_2 \Lambda_2^{(2)} & 0 & 0 & 1 \end{bmatrix} \begin{bmatrix} a_0 \\ a_1 \\ a_2 \\ b_0 \\ b_1 \\ b_2 \end{bmatrix} = \begin{bmatrix} D_0^a \\ 0 \\ 0 \\ D_0^b \\ 0 \\ 0 \end{bmatrix}, \tag{22}$$

where $C_m^a = j_m'(ka)/h_m^{(2)'}(ka)$, $C_m^b = j_m'(kb)/h_m^{(2)'}(kb)$, $D_m^a = -j\rho c v_m/h_m^{(2)'}(ka)$, and $D_m^b = -j\rho c u_m/h_m^{(2)'}(kb)$.

Assume for now that the two pulsating spheres are the same size. The acoustic pressure and intensity are calculated and compared to a calculation that does not consider the interaction between the two sources. The two sources are separated by one sound wavelength, resulting in $kr_o = 2\pi$. Let $k_a = k_b = 2$. The number 12 is chosen for the series truncation, so that a 24×24 matrix equation is formed. The results of this calculation, performed in MATLAB®, are illustrated in Figs. 2 and 3. It appears that the interaction between the two sources affects the intensity field in both magnitude and direction, and the change of the intensity field is more pronounced close to the sources where the interaction between the sources is strongest. Similar calculations are performed for two pulsating spheres of different sizes, i.e., $ka = 1.2$ and $kb = 0.7$ with $kr_o = 2\pi$. The results of these calculations will be presented in Section 3, along with the experimental data.

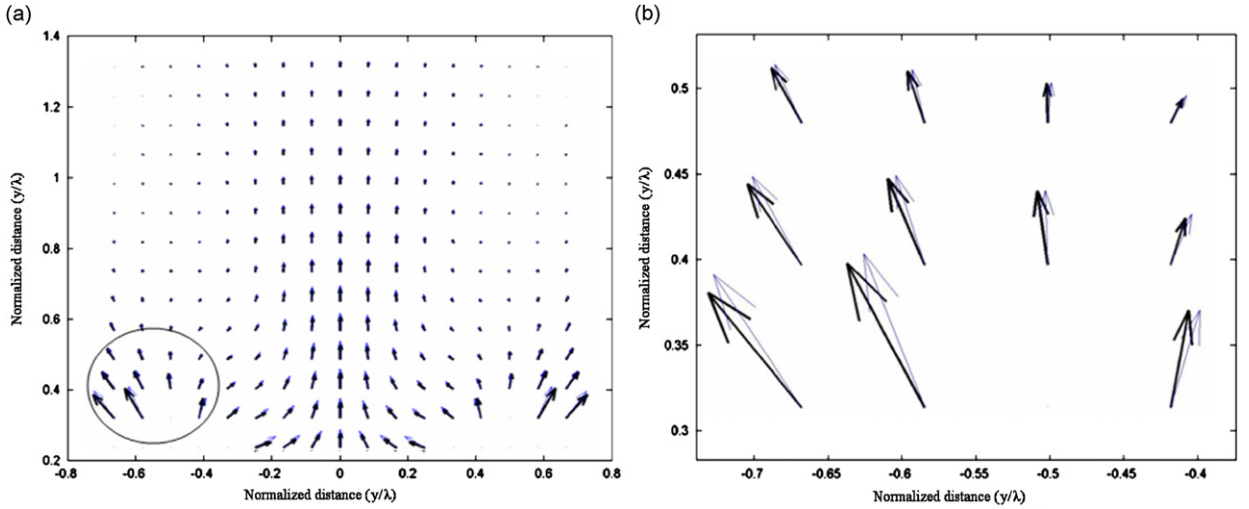

Fig. 2. (a). Active intensity field near two in-phase spherical sources separated by one wavelength, $kr_o = 2\pi$, and with $ka = kb = 2.0$. The length of the arrow is the linear intensity magnitude normalized by P_oV_o and its direction indicates the direction of energy flow. The fine-line arrows are for independent sources, and the heavy-line arrows are for interacting sources. The difference of the two is most pronounced near the sources where the interaction is strongest. The axes are unitless normalized by the wavelength, λ. Each source is centered at (−0.5,0) and (0.5,0). (b) A zoom of the circled region in (a).

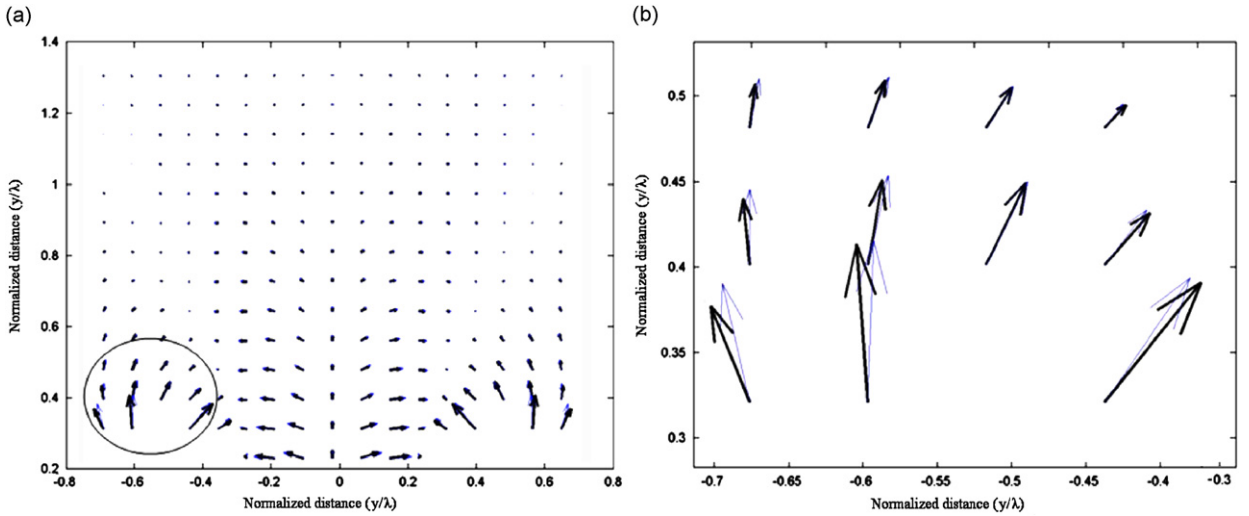

Fig. 3. (a). Computed reactive intensity field near the two spherical sources described in Fig. 2(a). The length of the arrow is the linear reactive intensity magnitude normalized by P_oV_o. Its direction is the direction of pressure change (gradient). The fine-line arrows are for the two independent sources, and the heavy-line arrows are for the interacting sources. The axes are unitless normalized by the wavelength, λ. Each source is centered at (−0.5,0) and (0.5,0). (b) A zoom of the circled region in (a).

3. Intensity measurements

3.1. Experimental setup

The experiments are performed in a 7.92 m long by 5.33 m wide by 5.49 m deep water tank (Fig. 4). The sound sources and the intensity probe were placed in the middle of the tank at a depth of 2.74 m. A block diagram of the measurement apparatus, including a plan view of the water tank setup and associated

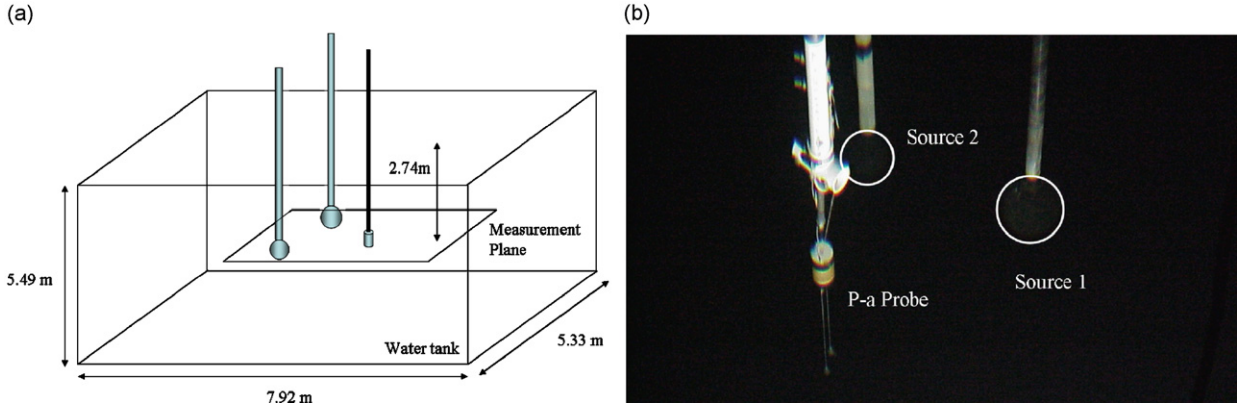

Fig. 4. The experimental setup. The sources were placed at the center of the tank. The box around the source and the probe in (a) represents the measurement plane. The picture of the probe and two sources is in (b). One of the sources was removed for the monopole experiment. Note the white circles mark the contours of the sources.

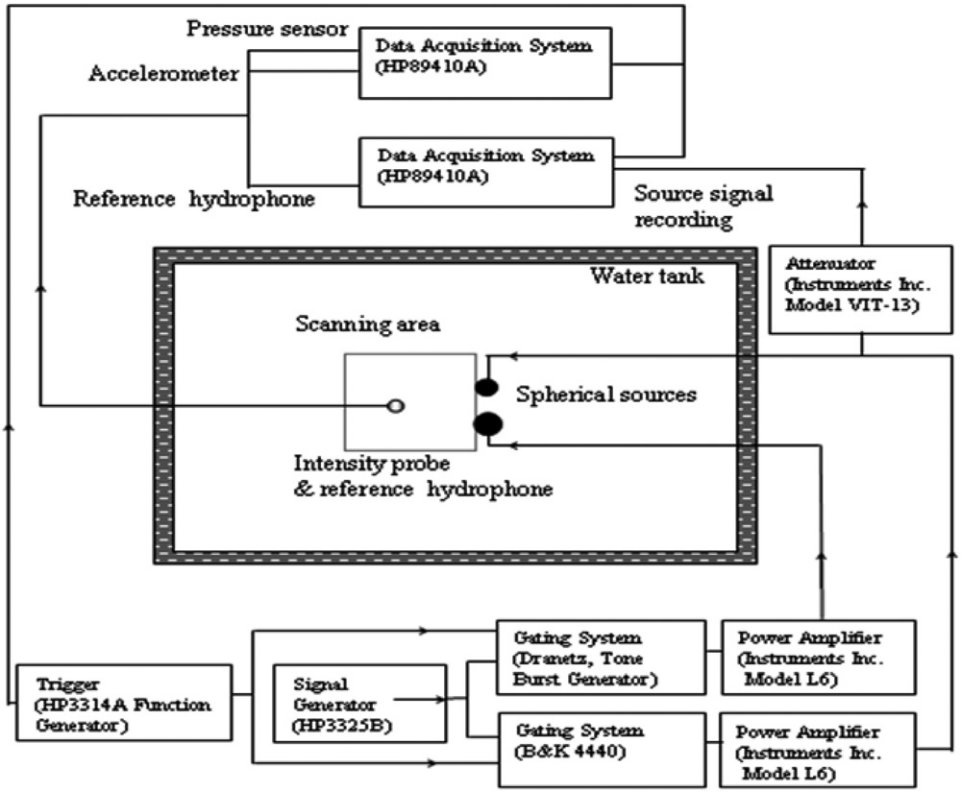

Fig. 5. Block diagram of the experimental system.

electronic equipment, is given in Fig. 5. A 10.8 cm diameter ITC1001 spherical transducer and a 6.86 cm diameter ITC1032 spherical transducer are used as the sound sources.

The transmitting equipment consists of a HP3325B signal generator, a HP3314A function generator, a Dranetz tone-burst generator, a B&K4440 gating system, and two Model L6 Instruments, Inc. power amplifiers. The HP3325B serves as a continuous sinusoidal signal generator. The Dranetz tone-burst generator and the B&K gating system gate the continuous sinusoidal signal according to the trigger signal generated by the HP3314A function generator. The transmitting trigger signal also synchronizes the data acquisition system. The Dranetz tone-burst generator drives the ITC1001 transducer, while the B&K gating system drives the ITC1032 transducer. The gated signal for each transducer goes through a power amplifier. To monitor the source driving voltage, the signal also goes into a data acquisition channel. The data-acquisition system consists of two HP89410A signal analyzers. One HP89410A is assigned to the p–a intensity probe [17] including the preamplifier. The other is connected to the reference hydrophone, with a preamplifier, and to the transducer driving signal. To prevent saturation within the HP89410A, the signals are attenuated by Model VIT-3 Instruments, Inc. attenuators. The HP89410 is set to gate the received direct signal and to calculate the cross-spectrum between pressure channel and acoustic particle acceleration channel.

The two projectors are attached to the ends of two poles supported directly above the water surface. The p–a intensity probe is connected, through a long pipe, to the actuating arm of a 3-D scanner (Parker, Inc.) controlled by a LabView® program.

The receiving beam pattern of the p–a intensity probe is also measured at discrete frequencies using a single spherical projector. In theory, the beam pattern of the pressure sensor in the plane orthogonal to the probe's cylindrical axis is omni-directional and the beam pattern of the accelerometer is dipole. The beam pattern of the intensity probe is the multiplication of these two patterns; it should be dipole. Deviation from this pattern indicates possible interference of the acoustic field due to diffraction by the probe itself, or to structural vibration modes in the probe body that are not completely cancelled by the accelerometer pair. For the subject probe operating at 5 kHz, *ka* value based on probe radius is 0.2, sufficiently smaller than unity which means that probe diffraction effects are negligible [10].

The p–a probe is mounted in a fixture that rotates in 5° increments, at a distance of 0.61 m from the ITC1032 projector. This transducer generates a gated, 4 ms long pulse. The received signal is gated to be 2 ms long in the middle of the 4 ms pulse, after the proper length of time has elapsed for the travel of the wave packet from the source to the receiver. The data acquisition system, HP89410A, is set to measure auto-spectra for the pressure and acceleration channels, and the cross-spectrum between them. The parameters of this processing are: bandwidth, 200 kHz; sampling frequency, 512 kHz; uniform window; 16 averages.

The beam pattern results are given in Fig. 6. The pressure beam pattern, determined from the output of the ceramic cylinder, is omni-directional in the horizontal plane, within a tolerance of ± 0.4 dB. The beam pattern of the accelerometer channel follows a dipole pattern to within a 0.4 dB difference between the forward and backward directions. It is suspected that this difference in sensitivity comes from an imbalance in the signal cable supporting the intensity probe. Testing the probe with different configurations of the supporting signal cable proved that the cable orientation and support could indeed cause this much of a difference in the fore-and-aft sensitivity. Based on these beam pattern data, and on the probe performance data reported previously [17], the overall accuracy of intensity data measured with this p–a intensity probe is estimated to be ± 1 dB for frequencies at or near 5 kHz.

3.2. Intensity near two closely spaced spherical sources

The acoustic intensity field produced by two interacting spherical sources is measured by the p–a intensity probe in a horizontal plane containing the sources in the water tank. Two different sizes of spherical hydrophones, the ITC 1001 and ITC 1032, are placed at a depth of 2.74 m in the middle of the tank. They are separated by one acoustic wavelength at 5 kHz, which is about 0.30 m. The scanner holds the intensity probe at the same depth as the sources and moves the probe sequentially in 5.1 cm increments in the x- and y-directions. The whole scanning field covers an area of 0.61×0.61 m. The data collection grid is illustrated in Fig. 7.

To determine the intensity vector at a certain point, one must measure the two components of intensity, in the x- and y-directions. Because the intensity probe developed for this research is a one-component sensor, the

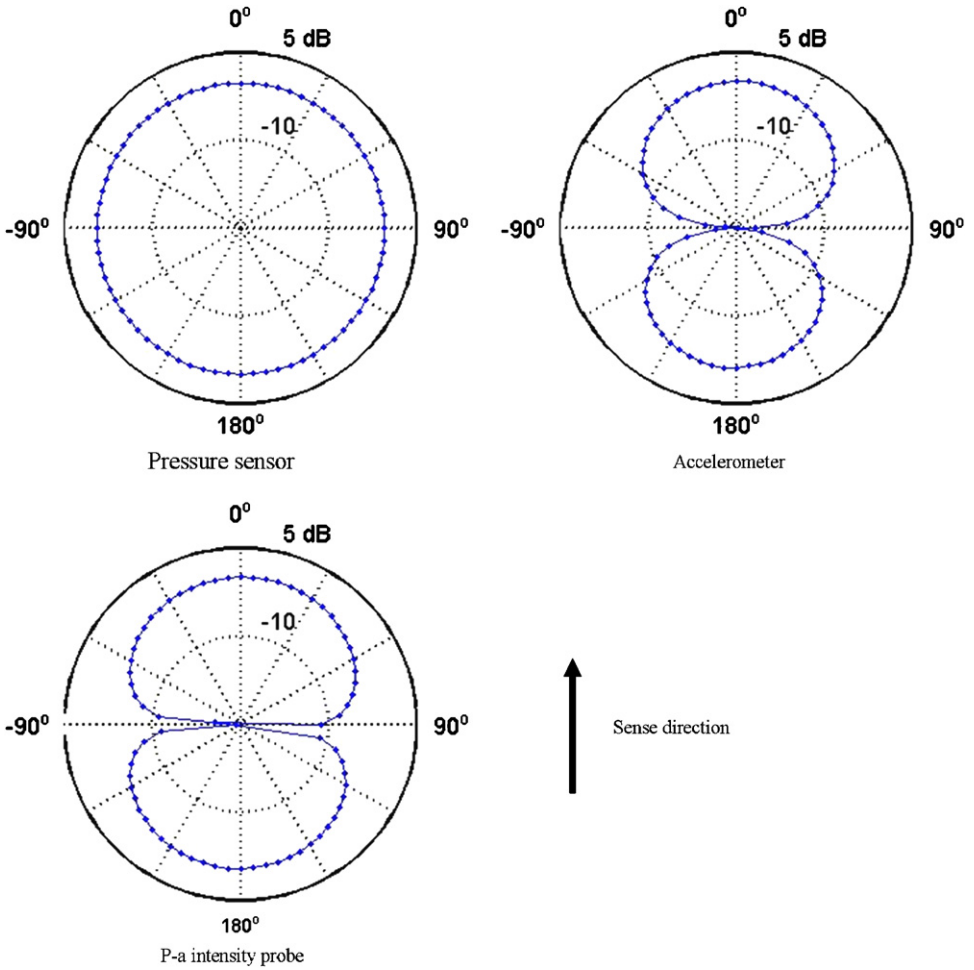

Fig. 6. Beam pattern of the p–a intensity probe at 5 kHz.The probe is 0.308 m ($kr = 12.8$) away from the source. The beam pattern of the ceramic cylinder is omni-directional in the horizontal plane, within ± 0.4 dB. The beam pattern of the accelerometer follows a dipole pattern with a 0.4 dB maximum difference between forward and backward direction. Dots represent data points and solid lines are connections between them.

probe needs to be rotated 90° to obtain the orthogonal component at each point. A 4 ms, gated-pulse of a 5 kHz sinusoidal signal drives the sources. For the sake of simplicity, the driving voltage to each source is adjusted until the sound pressure from each source at an arbitrary point, equal distance from the two sources, has the same value. To distinguish between the desired, direct path data and signals reflected from the walls and water surface, gated-pulse techniques are used in this experiment. The leading 2 ms of the received signal is gated, assuring that only the sound in the direct path is processed. The cross-spectrum between the gated pressure sensor output and the gated accelerometer output is used to determine the intensity.

The results for the single-source experiment are given in Figs. 8 and 9. The active intensity vector plot (Fig. 8) explicitly indicates the source location and the direction of the energy flow. The reactive intensity plot (Fig. 9) illustrates the pressure gradient distribution. Overall, the measurements agree well with the theoretical predictions. Note that the reactive intensity decreases faster with distance from the source than does the active intensity. This is expected for monopole sources because active intensity obeys an inverse square law while the reactive intensity obeys an inverse cube law. The directions of the measured vector intensity appear to be skewed to the left from those of the theoretical prediction. This is especially apparent at the centerline ($x = 0$) in the y-direction. In theory, the y-component of intensity along $x = 0$ must be zero. In practice, it was not easy to place the intensity probe precisely along the centerline of the source. Therefore, this likely probe

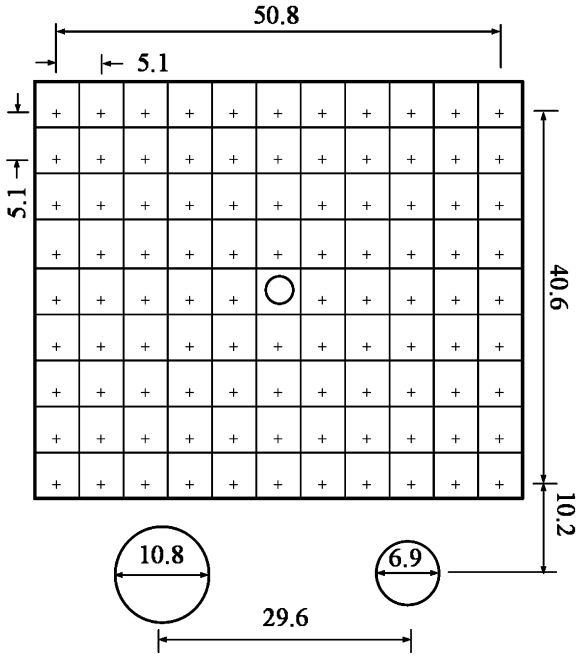

Fig. 7. The data collection grid in the x–y plane for the two-source experiment. The circles at the bottom of the figure represent the spherical sources: the ITC 1001 on the left, and the ITC 1032 on the right. The circle in the middle of the box represents the p–a intensity probe of diameter 3.8 cm. The closest data point to the source is limited by the access of the scanner above water relative to the pole holding the source. When single source was used, the closest measurement line is 12.7 cm away from the source and there are five points missing around the source from the grid. All dimensions are in cm.

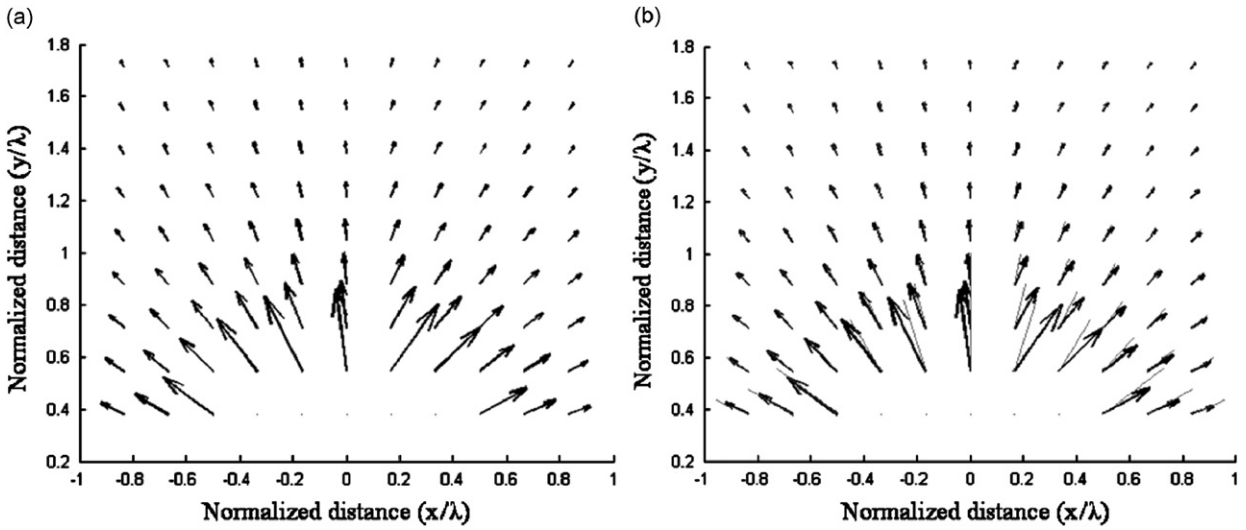

Fig. 8. Active acoustic intensity of a single spherical source ($kb = 0.7$). The upper plot (a) is the measurement and the lower plot (b) is the theoretical prediction overlaid on top of the measurement. The heavy lines with arrows are measurements corresponding (a) and the fine lines without arrows represent theoretical predictions. All the directions of theoretical predictions (lines without arrows) are pointing outward in the same way as measurements.

misalignment causes a small y-component of intensity to be measured. It causes the skewing of the intensity vectors to the left. This error is also present in the experiments involving two sources.

The measurements of the intensity for the case of two sources vibrating in phase with each other are illustrated in Figs. 10 and 11. The two sources are of different sizes, i.e., $ka = 1.2$, and $kb = 0.7$, and separated

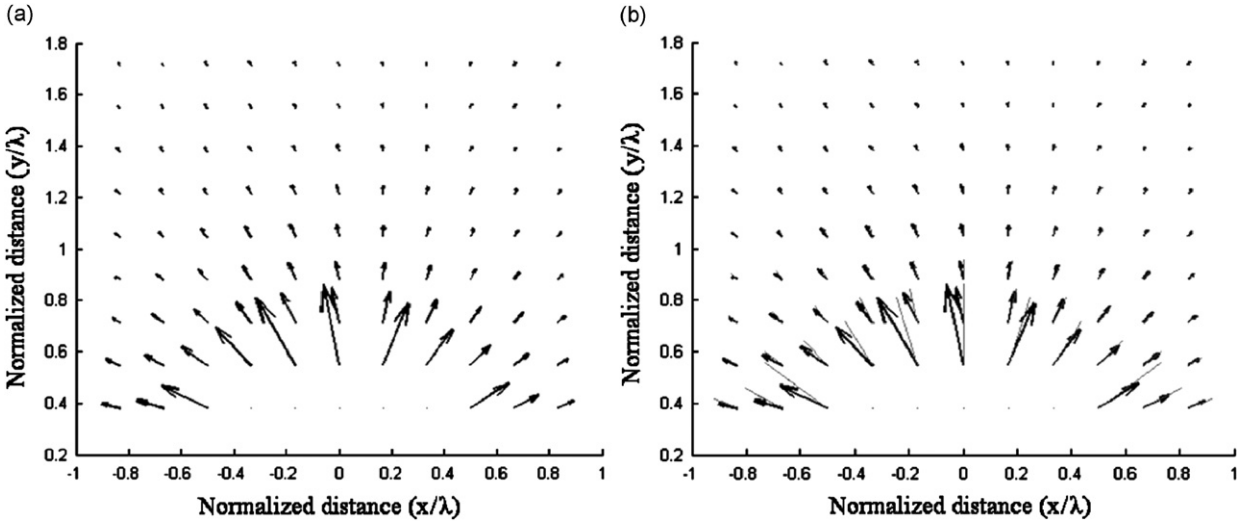

Fig. 9. Reactive acoustic intensity of a single spherical source ($kb = 0.7$). The format of the plots (a) and (b) are same as Fig. 8.

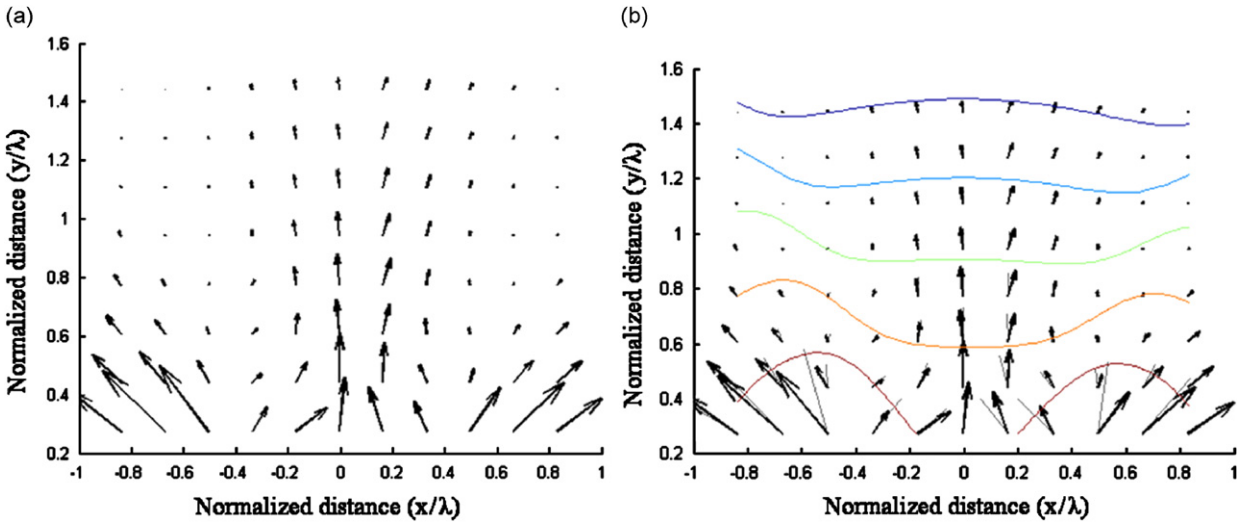

Fig. 10. Active intensity of two spherical sources vibrating in phase with each other ($ka = 1.2$, $kb = 0.7$, $kr_o = 2\pi$. The format of the plots (a) and (b) are the same as Fig. 8. The horizontal lines in the lower plot represent wavefronts. Note that the direction of active intensity is orthogonal to these lines of the constant pressure phase.

by one wavelength, i.e., $kr_o = 2\pi$. The pressure from two sources add constructively along the centerline ($x = 0$) in the y-direction. The measured intensity matches the predicted values, except at the centerline and very close to the source. At a distance as close as 10.16 cm ($\approx 0.3\lambda$) to the source at 5 kHz, there is also the possibility of interaction between the source and the intensity probe causing interference in the sound field. The vector plots of active and reactive intensity (Figs. 10 and 11, respectively) clearly distinguish the two sound sources and illustrate the pressure gradient distribution throughout the space.

Intensity measurements for two spherical sources vibrating 180o out of phase with each other are shown in Figs. 12 and 13. It is apparent from Fig. 12 active intensity that there is no acoustic energy propagating along the centerline ($x = 0$) in the y-direction where a pressure node is present. Two separate sources are identified. Fig. 13 illustrates that the reactive intensity produced by the two sources points predominantly away from the pressure maxima (or minima) and toward the pressure zeros (nodes). The length of the arrows are a measure

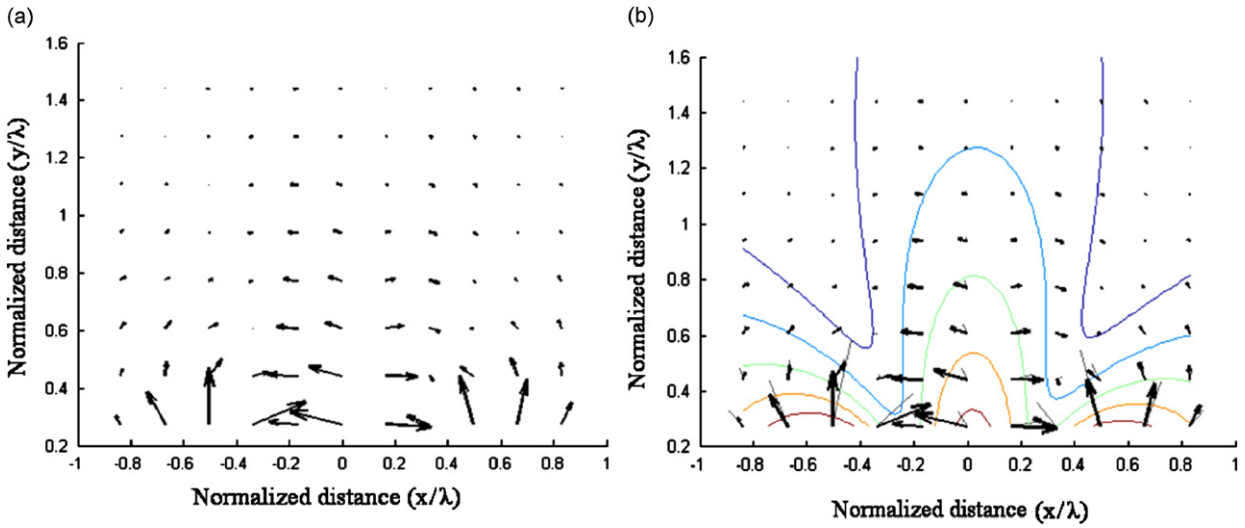

Fig. 11. Reactive intensity of two spherical sources vibrating in phase with each other ($ka = 1.2$, $kb = 0.7$, $kr_o = 2\pi$). The format of the plots (a) and (b) are the same as Fig. 8. The horizontal lines in the lower plot represent lines of constant pressure magnitude. Note that the direction of the reactive intensity is orthogonal to the lines of constant pressure, thus representing direction of pressure change.

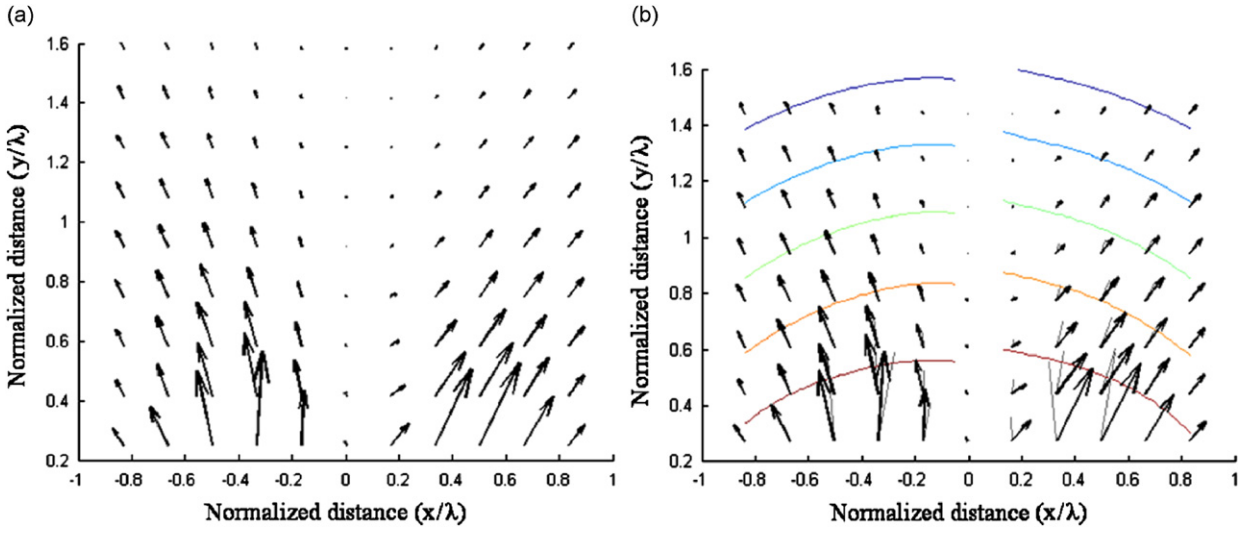

Fig. 12. Active intensity of two spherical sources vibrating 180o out of phase with each other ($ka = 1.2$, $kb = 0.7$, $kr_o = 2\pi$). The format of plots (a) and (b) are the same as Fig. 8. The horizontal lines in the lower plot represent lines of constant pressure phase.

of the magnitude of the gradient of the squared pressure. Along the pressure node, the opposing reactive intensities from the two sources cancel each other.

4. Summary and conclusions

In this paper, the characteristics of the acoustic intensity field near interacting acoustic sources have been examined both theoretically and experimentally. The underwater acoustic intensity field of a single spherical source was first measured to give a baseline for comparison to well-known solutions. Then, based on Thompson's work [18–20] on the scalar acoustic coupling between two non-compact spherical sources, new expressions for the acoustic vector intensity field of two closely spaced spherical sources was derived and

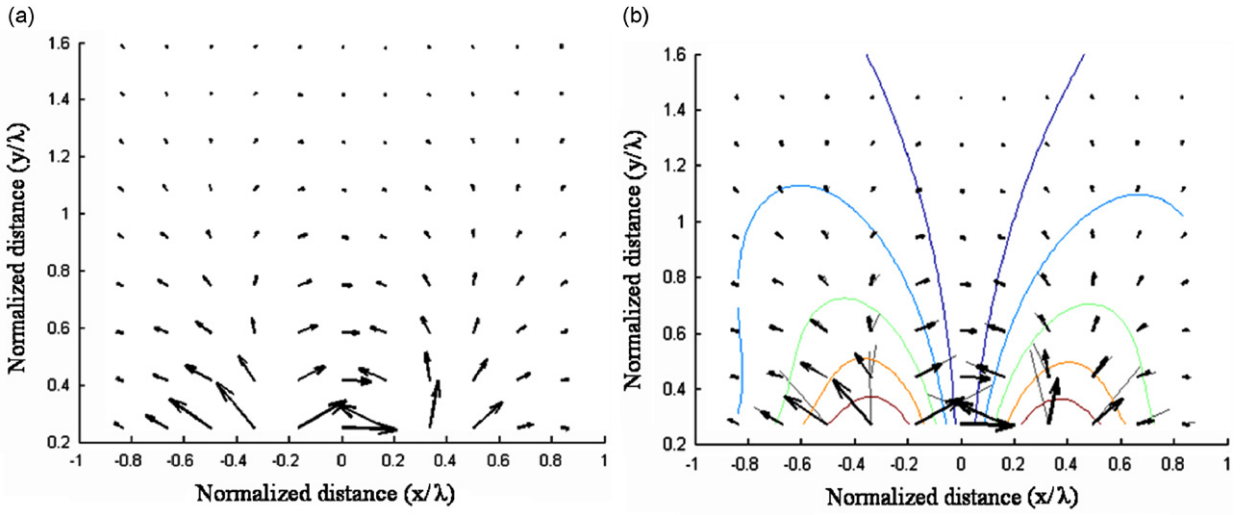

Fig. 13. Reactive intensity of two spherical sources vibrating 180° out of phase with each other ($ka = 1.2$, $kb = 0.7$, $kr_o = 2\pi$). The format of the plots (a) and (b) are the same as Fig. 8. The horizontal lines in the lower plot represent lines of constant pressure magnitude.

evaluated numerically. All measured intensities agree very favorably with the predicted values. The resulting intensity maps show the usefulness of underwater near-field intensity measurements in indicating source location, radiation patterns, and energy flow. Hence, the described p–a sensor may be confidently used to map the nearfield of more complicated underwater acoustic radiators to reveal localized regions of sound production. This radiation information is manifested in energy flow direction and in reactive regions of fluid oscillation. The favorable comparison of exact computational results with measurements has provided a degree of verification for the unique underwater acoustic intensity measurements performed. Based on intensity probe calibrations and measured beam patterns at 5 kHz, the described probe provides about ± 1 dB accuracy in intensity measurements. This accuracy can possibly be improved by a more careful design of the signal cables that exit the neutrally buoyant probe body.

Acknowledgements

This work has been supported by several grants from the Office of Naval Research (ONR), Code 321SS. They include an MURI Grant N00014-96-1-1173, and regular Grants N00014-00-1-0300 and N00014-01-1-0108. The support of program manager Dr. James F. McEachern is gratefully appreciated. The authors also greatly appreciate Applied Research Laboratory at Penn State for the experimental facility support.

References

[1] J.H. Enns, F.A. Firestone, Sound power density fields, *Journal of the Acoustical Society of America* 14 (1942) 24–32.
[2] R.H. Bolt, A.A. Petrauskas, An acoustic impedance meter for rapid field measurement, *Journal of the Acoustical Society of America* 15 (1943) 79(A).
[3] J.F. Burger, G.J.J. van der Merwe, G.B. van Zyl, L. Joffe, Measurement of sound intensity applied to the determination of sound power, *Journal of the Acoustical Society of America* 53 (1973) 1167–1168.
[4] B.F. van Zyl, F. Anderson, Evaluation of intensity method of sound power determination, *Journal of the Acoustical Society of America* 57 (1975) 682–686.
[5] S. Baker, Acoustic intensity meter, *Journal of the Acoustical Society of America* 27 (1955) 269–275.
[6] T.J. Schultz, Acoustic wattmeter, *Journal of the Acoustical Society of America* 28 (1956) 693–699.
[7] F.J. Fahy, Measurement of sound intensity using the cross-spectral density of two microphone sensors, *Journal of the Acoustical Society of America* 62 (1977) 1057–1059.
[8] J.Y. Chung, Cross-spectral method of measuring acoustic intensity without error caused by instrument phase mismatch, *Journal of the Acoustical Society of America* 64 (1978) 1613–1616.

[9] F.J. Fahy, *Sound Intensity*, second ed., E & FN SPON, an imprint of Chapman & Hall, London, UK, 1995.
[10] C.B. Leslie, J.M. Kendall, J.L. Jones, Hydrophone for measuring particle velocity, *Journal of the Acoustical Society of America* 28 (1956) 711–715.
[11] B. Bauer, A. DiMattia, Moving-coil pressure-gradient hydrophone, *Journal of the Acoustical Society of America* 39 (1966) 1264(A).
[12] G.L. D'Spain, W.S. Hodgkiss, G.L. Edmonds, Energetics of deep ocean's infrasonic sound field, *Journal of the Acoustical Society of America* 89 (1991) 1134–1158.
[13] T.B. Gabrielson, D.L. Gardner, S.L. Garrett, A simple neutrally buoyant sensor for direct measurement of particle velocity and intensity in water, *Journal of the Acoustical Society of America* 97 (1995) 2227–2237.
[14] T. B. Gabrielson, J. F. McEachern, G. C. Lauchle, Underwater acoustic intensity probe, US Patent No. 5,392,258, February 21, 1995.
[15] J.A. McConnell, Analysis of a compliantly suspended acoustic velocity sensor, *Journal of the Acoustical Society of America* 113 (2003) 1395–1405.
[16] K.J. Bastyr, G.C. Lauchle, J.A. McConnell, Development of a velocity gradient underwater acoustic intensity sensor, *Journal of the Acoustical Society of America* 106 (1999) 3178–3188.
[17] K. Kim, T.B. Gabrielson, G.C. Lauchle, Development of an accelerometer-based underwater acoustic intensity sensor, *Journal of the Acoustical Society of America* 116 (6) (2004) 3384–3392.
[18] W. Thompson Jr., Acoustic radiation and scattering from two eccentrically positioned spheres, PhD Thesis in Acoustics, The Pennsylvania State University, 1971.
[19] W. Thompson Jr., Radiation from a spherical acoustic source near a scattering sphere, *Journal of the Acoustical Society of America* 60 (4) (1976) 781–787.
[20] W. Thompson Jr., Acoustic coupling between two finite-sized spherical sources, *Journal of the Acoustical Society of America* 62 (1) (1977) 8–11.
[21] R.V. Waterhouse, Output of a sound source in a reverberation chamber and other reflecting environments, *Journal of the Acoustical Society of America* 30 (1958) 4–13.
[22] M.I. Karnovskii, Interaction acoustical impedance of spherical radiators and resonators, *C. R. (Dokl.) Acad. Sci. URSS* 32 (1941) 40–43.
[23] G. Krishnappa, Active intensity in the nearfield of two interfering monopoles, *Journal of the Acoustical Society of America* 74 (4) (1983) 1149–1154.
[24] S.Y. Ham, W.S. Kim, M.G. Prasad, Interference studies of acoustic pressure and intensity fields of two simple sources, *Journal of the Acoustical Society of America* 90 (2) (1991) 1149–1154.